Estimation of wind forcing and analysis of near-inertial motions generated by a storm in a submarine canyon with an ensemble Kalman filter

Antoni Jordi[1] and Dong-Ping Wang[2,3]

[1] IMEDEA (UIB-CSIC), Institut Mediterrani d'Estudis Avançats, Miquel Marquès 21, 07190 Esporles, Spain.

[2] State Key Laboratory of Satellite Ocean Environmental Dynamics, Second Institute of Oceanography, Hangzhou, China

[3] School of Marine and Atmospheric Sciences, Stony Brook University, Stony Brook, NY 11794, USA.

Abstract

The impact of high-frequency winds on the generation and propagation of inertial currents in the Palamós submarine canyon (northwestern Mediterranean) during a severe storm on 9-16 November 2001 is evaluated in an ocean circulation model. Moored current meter time series collected in and around the canyon during the storm are assimilated with an ensemble adjustment Kalman filter (EAKF) to adjust wind forcing through a simultaneous state and parameter estimation approach. Winds are included as time-dependent parameters, which are updated in each assimilation step as part of the model state. A simulation forced by the estimated wind significantly improves simulation with winds from the atmospheric reanalysis (the RMS error reduction is about 50%). This is due to the higher energy for the estimated wind at inertial period in the clockwise rotating component, which enhances generation of near-inertial motions. The surface inertial energy however does not decay as rapidly compared to a simulation with data assimilation. It is suggested that the submesoscales, which are present in the data assimilated simulation, are effective in channeling a spatially heterogeneous vertical propagation of near-inertial motions.

Keywords: Inertial currents; Kalman filters; Parameter estimation; High-frequency wind; Submesoscales; Mediterranean Sea

1. Introduction

Near-inertial motion and internal tides are believed to be efficient energy sources for small-scale mixing in the deep ocean, needed to maintain the meridional overturning circulation (Alford, 2003; Munk and Wunsch, 1998). Near-inertial energy is generated in the upper ocean in response to variable wind stress (Gill, 1984). The propagation of near-inertial waves depends on their horizontal scales. Several processes can contribute to reduce the initially large horizontal scales (because of the presumed wind scales) and thus to transfer the near-inertial energy from the upper ocean downward. For example, fronts and mesoscale eddies favor the vertical propagation of near-inertial energy from the surface to the deep ocean through refraction by the relative vorticity (D'Asaro, 1995; Kunze, 1985; Wang, 1991).

However, several studies have pointed out the impact of high-frequency and small-scale wind variability on the vertical propagation of near-inertial energy. The convergence or divergence in the wind field can give rise to near-inertial motions much larger (in magnitude) and shorter (in horizontal scale) than that due to steady large-scale winds (Greatbatch, 1983; Salat et al., 1992). Also, the rotation of wind forcing in concert with the inertial currents has been observed to produce dramatic resonant responses in the upper ocean (Large and Crawford, 1995). Both, the duration (with respect to the Coriolis period) and the rotation direction of the wind are important to reinforce the near-inertial energy (Skyllingstad et al., 2000). In this regard, Klein et al. (2004) demonstrated that at least three-hourly wind time series is required to generate intense near-inertial motion, independent of mesoscale eddy field.

Jordi and Wang (2008) had previously analyzed the vertical propagation of near-inertial energy generated by an extreme storm during 9-16 November 2001 in and around the Palamós submarine canyon, one of the major canyons that indent the continental margin of the Gulf of Lions and Catalan Sea in the northwestern Mediterranean (Jordi et al., 2005b). They used current meter data to demonstrate that near-inertial waves generated by the storm over the shelf and inside the canyon have significantly different characteristics from those in the open ocean. Based on model simulations, these differences were shown to be caused by the vorticity associated with the presence of a storm-generated alongshore jet. On the onshore side of the jet (inside the canyon), free near-inertial motions are rapidly carried away by normal inertial waves and dissipated by wave reflection off canyon walls. On the offshore side of the jet (outside the canyon), free near-inertial motions propagate first downward as anomalously low frequency internal waves and are then advected southward and offshore by the mean flow. Although the numerical model reproduced quite well the behavior of observed near-inertial motions, model underestimated the amplitude of near-inertial motions.

The objective of this study is to evaluate the impact of high-frequency/small-scale wind field previously not considered in Jordi and Wang (2008). The ocean circulation model and its configuration are the same as before. As there were no direct measurements of high-frequency wind variability during the storm, an ensemble Kalman filter (EnKF) is implemented to adjust the wind stress through the simultaneous state and parameter estimation approach. We treat the uncertainties of wind stress as parameters, i.e. as a part of the unknown model states, within the numerical model. In other words, we try to use current meter observations to constrain the forcing field. The EnKF is a widely used data assimilation method based on the integration of an ensemble of model states forward in time according to the model dynamics to predict error statistics needed for the assimilation (Evensen, 1994). The simultaneous state and parameter estimation approach combines standard model prognostic variables (regular model states) with parameters in an augmented state vector continuously updated through data assimilation

(Evensen, 2009; Lermusiaux and Robinson, 1999). Previous applications include estimation of boundary conditions, atmospheric forcing, and physical and biological parameters (Cossarini et al., 2009; Jordi and Wang, 2013; Lermusiaux, 1999).

2. Data and Methods

2.1. Numerical model

The model used in this study is a parallel version of the Princeton Ocean Model (POM), which is a terrain-following, free surface, primitive equation ocean circulation model (Blumberg and Mellor, 1987; Jordi and Wang, 2012). The model configuration is exactly the same as used in Jordi and Wang (2008), with the exception of wind forcing (see below). The model domain covers the Palamós canyon and adjacent areas in the western Mediterranean Sea, although the real topography is restricted to the area close to the canyon (Fig. 1). The maximum horizontal grid resolution is 1 km over the canyon head, with coarser resolution toward the offshore and alongshore boundaries. The vertical grid has 81 non-uniform sigma-levels concentrated toward the surface. The bathymetry is slightly smoothed to reduce the effect of pressure gradient errors to a tolerable level, and small-scale features are not fully resolved.

The model runs from 6 to 20 November 2001, encompassing the period of an extreme storm that lashed the western Mediterranean during 9-16 November 2001. The initial temperature and salinity fields are horizontally uniform with a pycnocline at around 100 m depth. The open boundaries are placed far from the canyon so that they do not affect the vertical propagation of near-inertial motions in the vicinity of the canyon for the limited time of model integration (14 days). The boundary conditions in the alongshore direction (northern and southern boundaries) are periodic for all variables, which avoids the uncertainty in open boundary conditions (Gan and Allen, 2005). On the offshore (eastern) boundary, a radiation condition is used for velocities, and an advective condition is used for temperature and salinity with the inflows set equal to the initial temperature and salinity.

Atmospheric forcing consists of wind stress and heat and fresh water fluxes provided at hourly interval by the Mediterranean hindcast of dynamic processes of the ocean and coastal areas of Europe (HIPOCAS) data set (Sotillo et al., 2005). HIPOCAS is a dynamical downscaling from the NCEP/NCAR global reanalysis (Kalnay et al., 1996) at a resolution of 0.5º × 0.5º over the Mediterranean Sea. Although the improvement of HIPOCAS winds versus global reanalysis datasets is significant, particularly in the characterization of extreme winds (Sotillo et al., 2005), the HIPOCAS wind lacks small-scale variability due to the coarser resolution. We therefore estimate new wind forcing fields through the simultaneous state and parameter estimation approach.

2.2. Simultaneous state and parameter estimation

In the EnKF approach, an ensemble of model states is integrated forward in time according to the model dynamics to predict error statistics needed for data assimilation and accordingly to correct the standard prognostic variables (Evensen, 1994). The simultaneous state and parameter estimation combines the standard prognostic variables with parameters in an augmented state vector, which is continuously updated through data assimilation with the EnKF method. The method was used in Jordi and Wang (2013) in which the boundary conditions are treated as parameters to study circulations in the Palma Bay. Here, wind stress components are treated as parameters and the simultaneous state and parameter estimation corrects the model state and provides an estimate of the wind forcing components. The particular EnKF approach used in this study is the ensemble adjustment Kalman filter (EAKF) (Anderson, 2001). Basically, the EAKF processes each scalar observation sequentially, so that its operation can be accomplished by describing only the impact of a single scalar observation on a single state vector. First, an ensemble of *N* model state vectors is integrated forward from the time of the previous observation to the time of the next available observation. Forecast (prior) estimates for this observation ($\mathbf{y}^{\mathrm{f}}$) are computed by applying the observation operator $\mathbf{H}$ to each forecast ensemble member of the single model state ($\mathbf{x}^{\mathrm{f}}$)

$$\mathbf{y}^{\mathrm{f}} = \mathbf{H}\mathbf{x}^{\mathrm{f}} \tag{1}$$

Given the scalar observed value $\mathbf{y}^{\mathrm{o}}$ with observational error covariance $\mathbf{R}$, the analysis (posterior) ensemble estimate for $\mathbf{y}$ is

$$\mathbf{y}^{\mathrm{a}} = \sqrt{\frac{\mathbf{P}^{\mathrm{a}}}{\mathbf{P}^{\mathrm{f}}}}\left(\mathbf{y}^{\mathrm{f}} - \overline{\mathbf{y}^{\mathrm{f}}}\right) + \overline{\mathbf{y}^{\mathrm{a}}} \tag{2}$$

where $\overline{\mathbf{y}^{\mathrm{f}}}$ and $\mathbf{P}^{\mathrm{f}}$ are the forecast ensemble mean and covariance, respectively. The analysis (posterior) ensemble mean ($\overline{\mathbf{y}^{\mathrm{a}}}$) and covariance ($\mathbf{P}^{\mathrm{a}}$) are

$$\overline{\mathbf{y}^{\mathrm{a}}} = \mathbf{P}^{\mathrm{a}}\left(\frac{\overline{\mathbf{y}^{\mathrm{f}}}}{\mathbf{P}^{\mathrm{f}}} + \frac{\mathbf{y}^{\mathrm{o}}}{\mathbf{R}}\right) \tag{3}$$

$$\mathbf{P}^{\mathrm{a}} = \left[\left(\mathbf{P}^{\mathrm{f}}\right)^{-1} + \left(\mathbf{R}\right)^{-1}\right]^{-1} \tag{4}$$

Then each ensemble member for the state variable is updated by doing a linear regression of the observation space increments ($\mathbf{y}^{\mathrm{a}}$-$\mathbf{y}^{\mathrm{f}}$) onto the state vector component using the forecast joint ensemble sample statistics

$$\mathbf{x}^{\mathrm{a}} = \mathbf{x}^{\mathrm{f}} + \frac{\mathbf{P}_{\mathbf{x},\mathbf{y}}}{\mathbf{P}^{\mathrm{f}}}\left(\mathbf{y}^{\mathrm{a}} - \mathbf{y}^{\mathrm{f}}\right) \tag{5}$$

where $\mathbf{P_{x,y}}$ is the forecast sample covariance between the model states $\mathbf{x}^f$ and $\mathbf{y}^f$, determined directly from the ensemble. This algorithm is sequentially applied for each scalar observation and augmented model state variable. To increase the computational efficiency, a parallel implementation of the EAKF algorithm is used (Anderson and Collins, 2007).

2.3. Generation of ensemble members

The EAKF requires an ensemble of model states for initialization. We generate 32 ensemble members by setting randomly an alongshore (*y*-direction) barotropic flow at model initialization, taken from a uniform distribution ranged from –0.05 to 0.05 m s^{-1}. In addition, the wind forcing is perturbed following Vandenbulcke et al. (2008). The wind is first decomposed as sums of EOFs and then summed back with the weights of the decomposition multiplied by a random coefficient ranged from 0.6 to 1.4. The corresponding root mean square (RMS) of the perturbed wind field is 2.5 m s^{-1}. No other fields (heat and water fluxes, boundary conditions…) are perturbed.

2.4. Model runs

Three runs are conducted to assess the effect of simultaneous state and parameter estimation. These runs include:

- BASE: The simulation is forced by the HIPOCAS wind forcing and does not include data assimilation. It is used as a benchmark.
- ASES: The BASE + EAKF performs a simultaneous assimilation and parameter estimation. The assimilation affects the augmented state vector, composed of the standard prognostic variables and wind forcing components (parameters). The

data assimilation produces a best estimate of the flow field. It also generates a new estimated wind forcing that is consistent with the observations.

- ESTIM: The simulation is the same as BASE except that it is forced by the estimated wind from the ASES run.

2.5. Data

Observational data consists of velocity time series collected inside and in the vicinity of the Palamós canyon (Fig. 1). The main features of observed currents are described in detail by Palanques et al. (2005). Here we assimilate 12 velocity time series, including two from an upward-looking acoustic Doppler current profiler (ADCP) and 10 from moored current meters (Table 1). Although the ADCP covered the water column from 256 to 488 m depth, only currents measured at top and bottom ADCP levels are assimilated, and currents at other depths are used to validate the model results. Following Palanques et al. (2005), data are separated for convenience into two groups: upper level (150–279 m) and intermediate level (401–506 m). The currents are rotated into the ocean model grid components and averaged at 1 h interval, corresponding to the assimilation time step in the EAKF. The observational error used in the assimilation is set to 0.01 m s^{-1}.

The observational data and model outputs are used to compute daily mean currents and inertial rotary components (Brink, 1989; Qi et al., 1995):

$$u + iv \approx a + be^{i(ft+\phi_b)} + ce^{-i(ft+\phi_c)} \qquad (6)$$

where u and v are the eastward and northward velocity components, f is the inertial frequency, t is the time, a is the sub-inertial component, b (c) is the counterclockwise (clockwise) amplitude, and ϕ_b (ϕ_c) is the counterclockwise (clockwise) phase. The variables a, b, ϕ_b, c and ϕ_c are evaluated using a least squares fit in a daily data window. The clockwise component is analyzed here for evidence of free-propagating near-inertial oscillations as inertial currents rotate clockwise in the Northern Hemisphere. We also apply this decomposition to scalar fields (e.g., density) using only the real part of Eq. 6.

3. Results

3.1. Model assessment

In this section the model results for the different runs are verified by comparison with the moored current meter data (assimilated) and the ADCP data (non-assimilated). To quantify the model skill in reproducing the observed currents, two metrics are introduced: the RMS error and the complex correlation coefficient between the observations and model results for each velocity time series. Table 2 summarizes the main results of this verification for sub-inertial and near-inertial currents. The overall RMS is 0.12, 0.01, and 0.06 m s^{-1} for BASE, ASES and ESTIM, respectively; and the overall correlation is 0.40, 0.94, and 0.57, respectively. The ASES has the best performance, as the data assimilation uses the same observations. Notably, ESTIM shows significant improvement over BASE in terms of both RMS and correlation. This suggests potential benefits of using refined wind forcing derived from an inverse modeling.

Figure 2 compares the mean sub-inertial observed currents for the studied period with those from the different runs. The observed sub-inertial currents at the upper level show an alongshore jet that flows from northeast to southwest. This jet is part of the Northern Current, a permanent density front in the region (Font et al., 1988). At the intermediate level, the observed currents are weaker and variable in direction as the Northern Current is typically confined to the upper 300 m of the water column. The different model runs indicate the presence of an alongshore jet despite that the initial condition does not include a density front (temperature and salinity are horizontally uniform). However, in BASE, the sub-inertial currents are more than twice as large as the observed currents and the alongshore jet reaches the intermediate level. In ESTIM, the sub-inertial currents are comparable to the observed currents, but the alongshore jet is less apparent. ASES assimilates the same observations, and is virtually identical to the observed (see also metrics in Table 2).

The main interest in this study is on the inertial currents. The near-inertial (clockwise) currents at upper level for the BASE, ASES and ESTIM are compared with the observations in Fig. 3. The vector length indicates the amplitude of near-inertial motion, vector direction is the relative phase, and dot is the vector origin. The observations show large near-inertial oscillations outside the canyon (M7-M8), and smaller and less coherent inertial currents inside the canyon (M3-M6). According to Jordi and Wang (2008), this lack of coherence is caused by wave reflection off canyon walls. In the BASE run, the near-inertial motions are underestimated. In ASES, both magnitude and phase of near-inertial currents are essentially the same as the observations. In ESTIM, while the magnitude of near-inertial currents is comparable to the observations, there are differences in the relative phase.

At the intermediate level, the observed near-inertial currents are weaker than in the upper level, and again they are larger outside the canyon (M7-M8) than inside (Fig. 4). In BASE, there is little evidence for near-inertial motions, particularly outside the canyon. ASES again agrees quite well with the observations. ESTIM displays near-inertial oscillations that are generally larger, especially inside the canyon (M3-M6), and out-of-phase with respect to the observations. The tendency that ESTIM has larger inertial currents than the observations is also evident at the upper level for M5-M8 (Fig. 3).

In the comparisons so far, the current meter data are not independent of the ASES and ESTIM runs. ASES assimilated the data and ESTIM used the estimated wind forcing from ASES. Therefore, we also compare the model runs with the ADCP data at M6 (Fig. 5). This is a more critical comparison, because ADCP data, except for the top and bottom levels, are not included in the model runs. The observations display a very complex vertical structure. BASE severely underestimates the inertial currents. In ESTIM, near-inertial currents are smaller than the observations at the beginning (November 12-15), but become much larger later on November 17-21. In contrast, the agreement between ASES and observations is outstanding.

A quantitative comparison of RMS error and correlation between the observed near-inertial current at the ADCP and the different model runs is shown in Fig. 6. The top and bottom ADCP levels are excluded from the comparison. For ASES, the RMS error is always less than 0.02 m s^{-1} and the correlation greater than 0.85. The RMS error in ESTIM is less than BASE, except in the bottom ADCP bins (below 430 m). ESTIM has also better correlation than BASE, except for a couple of bins around 300 m depth. Both ESTIM and BASE show a pronounced decrease in correlation between 300 and 340 m, which coincides with the maxima in observed near-inertial amplitude on November 12-17 (Fig. 5). These maxima are not reproduced neither by ESTIM nor BASE.

In Fig. 5, it is obvious that ESTIM has larger vertical length scales than the observations. To quantify changes in the vertical structure, the vertical wavenumber spectrum for the eddy kinetic energy (EKE) is obtained from the observed and simulated ADCP data at M6. We calculate the EKE as $(u'^2 + v'^2)/2$, where u' and v' are the velocity anomaly components estimated from inertial signals using Eq. 6. Fig. 7 shows near-inertial EKE spectra. ASES is in excellent agreement with the observations, showing comparable spectral energy and shape. ESTIM contains more energy than the observation for the larger wavelengths, but its spectrum drops sharply for vertical wavelengths smaller than 100 m. For BASE, the energy level is substantially less compared to the observations.

The model results are insensitive to variations in the setup of the EAKF. Although Jordi and Wang (2008) found differences in the magnitude of near-inertial motions associated with the initial temperature and salinity profiles, the velocity and the estimated wind from ASES remain basically the same as the EAKF is capable of correcting the entire model state including temperature and salinity. Increasing the number of ensembles up to 128 does not significantly alter the results. Other parameters such as localization and inflation are usually used in EnKF studies. The localization of observations avoids large correction at long distances from the observation. However, our results are similar for localized observations with cut-off distances greater than 15 km. Jordi and Wang (2013) used an inflation factor to keep the posterior and prior variances of parameters equal. In this study, the parameter (wind) variance is introduced in the generation of the ensemble members through the wind perturbation. At each model time step, wind is interpolated between past (estimated) and future (perturbed) wind forcing. This ensures the variance in wind stress, and there is no need of inflation.

3.2.Wind stress characteristics

In the previous section, we demonstrated that ESTIM is better than BASE in terms of the RMS error and the complex correlation coefficient. Since the only difference between these two runs is the wind forcing, we analyze here their respective wind fields. Winds evolve in accordance with the formation and evolution of a very deep cyclone over the western Mediterranean basin (Santos-Muñoz et al., 2006; Thomas et al., 2003). In the Palamós canyon area, HIPOCAS winds (used in BASE) are towards the southeast during the cyclone formation (November 9) and rotate to the southwest during its development (November 10 and 11), reaching a first wind stress maximum of about 1.4 N m^{-2} (Fig. 8). From November 11 to 13, the cyclone moves away to the east while local winds rotate to the southeast and relax. On November 14, the cyclone retreats back and winds in the Palamós canyon are again intensified up to 1.5 N m^{-2} and rotate to the southwest.

The estimated wind behaves similar to HIPOCAS wind with two wind maxima and comparable spatial patterns (Fig. 8). However, the first wind maximum is less intense (1.0 N m^{-2}), the second one is stronger (1.7 N m^{-2}), and the spatial pattern is slightly more uniform. Another remarkable difference between BASE and ESTIM winds is the high-frequency oscillations in the estimated winds. The less intense first maximum in the estimated wind is responsible for the reduced southward sub-inertial flow in ESTIM compared to BASE (Fig. 2). However, it does not seem likely that the reduced wind could be responsible for the larger inertial motion in ESTIM. It is well known that the clockwise rotation of the wind (in the Northern Hemisphere) at near-inertial frequencies is more effective for generation of inertial currents (Large and Crawford, 1995; Skyllingstad et al., 2000). The most distinctive example regarding this effect of wind rotation is the asymmetry in the near-inertial motions between the two sides of hurricane tracks (D'Asaro et al., 1995; Teague et al., 2007). Fig. 9 shows the spectral density for the clockwise rotation of the HIPOCAS and estimated winds. Whereas a significant peak at the inertial frequency is observed for the estimated wind, the peak is almost nonexistent for the HIPOCAS wind.

The parameter estimation through the EAKF introduces oscillations at the inertial frequency in the wind stress. To confirm that these wind oscillations are responsible for the increase of near-inertial motions in the ocean, we calculate the wind power input to near-inertial motions using $\boldsymbol{\tau_i}\cdot\boldsymbol{u_i}$, where wind stress $\boldsymbol{\tau_i}$ and surface current $\boldsymbol{u_i}$ are both near-inertial components estimated by filtering the time series at the inertial frequency. The HIPOCAS wind power input into the near-inertial currents for BASE averaged in space and time is −1.28 mW m^{-2}. The negative sign indicates that wind works against near-inertial currents. In contrast, the estimated wind power input into the near-inertial currents for ESTIM is 0.41 mW m^{-2}.

3.3.Propagation of near-inertial motions

In this section, we analyze the differences on the generation and propagation of near-inertial motions between ESTIM and ASES. The storm generates large near-inertial motions as well as an alongshore jet (Figs. 2-5). In regions of negative background vorticity where near-inertial wave's intrinsic frequency can be less than the effective frequency of the surrounding ocean, surface near-inertial energy can be effectively channeled downward (Kunze, 1985). Therefore, the background vorticity might play an important role in concentrating near-inertial motions in small-scale structures. On the other hand, it seems unlikely that the model could simulate the complex background vorticity field, due to the lack of initial temperature/salinity and velocity conditions. As the model deficiency could be partially compensated through data assimilation, ASES might produce a more realistic background vorticity field consistent with the observed structure of near-inertial motions.

Fig. 10 shows the time evolution of near-inertial currents and sub-inertial vorticity and density fields at a cross-shore section located at the canyon axis for ESTIM. On November 11, as a consequence of the storm, an Ekman coastal downwelling flow deepens the isopycnals near the canyon head and forms an alongshore jet. This pattern persists until the second wind maximum when upwelling flow develops near the canyon head and the center of the alongshore jet (defined by the 28.2 σ_θ isopycnal) moves progressively offshore. Development of upwelling and downwelling structures in the Palamós canyon as a consequence of the on- and offshore jet displacements was also found in a previous model study (Jordi et al., 2005b).

Inside the canyon (onshore side of the jet), the near-inertial energy has a patchy nature. The complex pattern of relative vorticity due to the interaction of the alongshore jet with the canyon topography would affect the propagation of near-inertial motion. Also, Jordi and Wang (2008) showed that most of near-inertial energy inside the canyon disappears in a few hours due to wave reflection with canyon topography. On the offshore side of the jet, near-inertial currents at surface rapidly move downward and are retained fairly uniform in the surface mixed layer. Normal near-inertial motions could not penetrate deeper because the vorticity is generally zero or positive (Kunze, 1985). However, small amplitude near-inertial motions are observed below the pycnocline. The downward transfer is associated with the presence of the sloping density jet, which allows anomalously free near-inertial waves propagate downward despite the counterclockwise rotation with depth (Mooers, 1975). Once anomalously near-inertial waves have penetrated through the pycnocline, they are free to spread away horizontally (Wang, 1991). The estimated exponential decay timescale of surface near-inertial energy after the second maximum is 19.3 days.

The vertical propagation of near-inertial currents and the associated sub-inertial vorticity and density fields for ASES are shown in Fig. 11. Similar to ESTIM, the onset of storm deepens the isopycnal near the coast. However, the upwelling after the second wind maximum found in ESTIM does not occur in ASES. Also, the density and vorticity fields, especially in the open ocean, have much more small-scale variability than in ESTIM. Consequently, near-inertial motions in the mixed layer are less uniform in ASES than in ESTIM. The near-inertial motions penetrate below the pycnocline as anomalously near-inertial waves through the sloping density jet after the two wind maxima. Vertical propagation as normal inertial waves (upward phase and downward energy propagation) is also observed after the first wind maximum in the open ocean (x > 80 km) as the vorticity is mainly negative. The estimated exponential decay timescale after the second maximum is 9.9 days. Inside the canyon, the pattern of near-inertial motions is incoherent as in ESTIM.

4. Discussion

In ASES, the background vorticity field is marked by intense, small-scale variability. The question to elucidate is whether submesoscales in ASES are generated by a real physical mechanism or are an artifact of the data assimilation. It is well known that instability and frontogenesis in the real ocean favor the development of submesoscale structure in the presence of horizontal density gradients (Mahadevan and Tandon, 2006; Mahadevan et al., 2010). In fact, the general circulation in the area of the Palamós canyon is dominated by a shelf/slope density front (Font et al., 1998; Jordi et al., 2005a). Meanders, filaments and eddies occur frequently associated with the shelf/slope density front (Flexas et al., 2002; Wang et al., 1988).

In previous submesoscale model studies, it is shown that very high model resolution (≤ 1 km) is required to produce realistic submesoscale (Capet et al., 2008; Wang and Jordi, 2011). This is not practical in EnKF, which requires a large number of model ensembles. Moreover, we are primarily interested in the storm response, and therefore have restricted the duration of model simulation. Despite these model limitations, we try to test the role of submesoscales in the propagation of near-inertial motions by imposing submesoscale structures at model initialization. In this new run (SUBMS), pseudorandom (spatially coherent) fields with length scales smaller than 10 km are added to the initial temperature and salinity fields at surface, following Evensen (1994). The variances of the perturbations of temperature and salinity are 2ºC and 0.4 psu, respectively. These surface perturbations are projected to the water column decreasing with depth until the thermocline where the perturbations are set to zero. The geostrophic currents associated with the new temperature and salinity fields are calculated prior to the first time step. Besides this initially imposed submesoscales, SUBMS is identical to ESTIM.

Fig. 12 shows time evolution of near-inertial currents and sub-inertial vorticity and density fields at a cross-shore section located at the canyon axis for SUBMS. There are small-scale structures; however they are larger than that in ASES and tend to disappear after the second wind maxima. This is somehow expected because the model resolution is too coarse. Nevertheless, the impact of these submesoscale structures on the near-inertial motions is significant. Compared to ESTIM, inertial currents above the thermocline are weaker and less spatially coherent for SUBMS. The vertical propagation through this imposed submesoscales produces a decrease of inertial energy in the surface mixed layer. The decay timescale of surface near-inertial motions for SUBMS is 10.4 days, which is comparable to the 9.9 days for ASES.

5. Conclusions

This study highlights the role of high-frequency winds and submesoscales on the generation and propagation of inertial currents. It is well known that the wind rotation in concert with the near-inertial motions amplifies the near-inertial energy (D'Asaro et al., 1995; Large and Crawford, 1995). However, the use of simultaneous state and parameter estimation through the EAKF to determine the optimal wind forcing is perhaps unique among all previous studies of the relationship between winds and near-inertial motions. Parameter estimation is thus a promising approach in dealing with the uncertainty of high frequency winds in ocean models. We note that the parameter estimation approach can be easily extended to other parameters such as open boundary conditions and bottom friction.

Previous studies have identified the importance of submesoscales structures in modulating the vertical exchange of water in the mixed layer and the horizontal exchange of water mass across a thermohaline front (Mahadevan and Tandon, 2006; Wang and Jordi, 2011). Our results indicate that submesoscales might be also crucial in channeling inertial energy from surface to the deep ocean. This is suggested through the assimilation of observed velocity time series in the model (ASES). The SUBMS run also seems to confirm this fact. Klein et al. (2004) found that small-scale oceanic structures disperse and aggregate near-inertial motions leading to spatially heterogeneous vertical propagation, in agreement with our results. Our model however has several limitations (initial uniform density field, short time integration, and coarse model resolution) to produce realistic submesoscales. More detailed studies are needed to test the hypothesis that the ubiquitous submesoscales provide a conduit for inertial energy into the ocean interior.

Acknowledgments

This research utilized resources at the New York Center for Computational Sciences at Stony Brook University/Brookhaven National Laboratory which was supported by the U.S. Department of Energy under Contract No. DE-AC02-98CH10886 and by the State of New York. This work was partially carried out in the framework of the CANYONS project, funded by the "Dirección General de Enseñanza Superior e Investigación Científica" (MAR1999-1060). The authors gratefully thank all the personnel involved in the CANYONS project and surveys. A. Jordi's work was supported by a Ramón y Cajal grant from the Spanish Ministry of Economy and Competitiveness. The HIPOCAS data set was kindly provided by Puertos del Estado.

References

Alford, M.H., 2003. Redistribution of energy available for ocean mixing by long-range propagation of internal waves. Nature 423, 159-162.

Anderson, J.L., 2001. An ensemble adjustment Kalman filter for data assimilation. Mon Weather Rev 129, 2884-2903.

Anderson, J.L., Collins, N., 2007. Scalable implementations of ensemble filter algorithms for data assimilation. J Atmos Ocean Tech 24, 1452-1463.

Blumberg, A.F., Mellor, G.L., 1987. A description of a three-dimensional coastal ocean circulation model, in: Heaps, N.S. (Ed.), Three-Dimensional Coastal Ocean Models. American Geophysical Union, Washington, DC, pp. 1-16.

Brink, K.H., 1989. Observations of the Response of Thermocline Currents to a Hurricane. J Phys Oceanogr 19, 1017-1022.

Capet, X., Mcwilliams, J.C., Mokemaker, M.J., Shchepetkin, A.F., 2008. Mesoscale to submesoscale transition in the California current system. Part I: Flow structure, eddy flux, and observational tests. J Phys Oceanogr 38, 29-43.

Cossarini, G., Lermusiaux, P.F.J., Solidoro, C., 2009. Lagoon of Venice ecosystem: Seasonal dynamics and environmental guidance with uncertainty analyses and error subspace data assimilation. J Geophys Res-Oceans 114, doi:10.1029/2008JC005080.

D'Asaro, E.A., 1995. Upper-ocean inertial currents forced by a strong storm. Part III: Interaction of inertial currents and mesoscale eddies. J Phys Oceanogr 25, 2953-2958.

D'Asaro, E.A., Eriksen, C.C., Levine, M.D., Niiler, P., Paulson, C.A., Vanmeurs, P., 1995. Upper-Ocean Inertial Currents Forced by a Strong Storm .1. Data and Comparisons with Linear-Theory. J Phys Oceanogr 25, 2909-2936.

Evensen, G., 1994. Sequential data assimilation with a nonlinear quasi-geostrophic model using Monte-Carlo methods to forecast error statistics. J Geophys Res-Oceans 99, 10143-10162.

Evensen, G., 2009. The Ensemble Kalman Filter for Combined State and Parameter Estimation: Monte Carlo Techniques for Data Assimilation in Large Systems. Ieee Control Systems Magazine 29, 83-104.

Flexas, M.M., de Madron, X.D., Garcia, M.A., Canals, M., Arnau, P., 2002. Flow variability in the Gulf of Lions during the MATER HFF experiment (March-May 1997). J Marine Syst 33, 197-214.

Font, J., Millot, C., Salas, J., Julia, A., Chic, O., 1998. The drift of modified Atlantic water from the Alboran Sea to the eastern Mediterranean. Sci Mar 62, 211-216.

Font, J., Salat, J., Tintoré, J., 1988. Permanent features of the circulation in the Catalan Sea. Oceanol Acta 9, 51-57.

Gan, J.P., Allen, J.S., 2005. On open boundary conditions for a limited-area coastal model off Oregon. Part 1: Response to idealized wind forcing. Ocean Model 8, 115-133.

Gill, A.E., 1984. On the Behavior of Internal Waves in the Wakes of Storms. J Phys Oceanogr 14, 1129-1151.

Greatbatch, R.J., 1983. On the Response of the Ocean to a Moving Storm - the Non-Linear Dynamics. J Phys Oceanogr 13, 357-367.

Jordi, A., Orfila, A., Basterretxea, G., Tintoré, J., 2005a. Coastal trapped waves in the northwestern Mediterranean. Cont Shelf Res 25, 185-196.

Jordi, A., Orfila, A., Basterretxea, G., Tintoré, J., 2005b. Shelf-slope exchanges by frontal variability in a steep submarine canyon. Prog Oceanogr 66, 120-141.

Jordi, A., Wang, D.-P., 2008. Near-inertial motions in and around the Palamos submarine canyon (NW Mediterranean) generated by a severe storm. Cont Shelf Res 28, 2523-2534.

Jordi, A., Wang, D.-P., 2013. Estimation of transport at open boundaries with an ensemble Kalman filter in a coastal ocean model. Ocean Model 64, 56-66.

Jordi, A., Wang, D.P., 2012. sbPOM: A parallel implementation of Princenton Ocean Model. Environmental Modelling & Software 38, 59-61.

Kalnay, E., Kanamitsu, M., Kistler, R., Collins, W., Deaven, D., Gandin, L., Iredell, M., Saha, S., White, G., Woollen, J., Zhu, Y., Chelliah, M., Ebisuzaki, W., Higgins, W., Janowiak, J., Mo, K.C., Ropelewski, C., Wang, J., Leetmaa, A., Reynolds, R., Jenne, R., Joseph, D., 1996. The NCEP/NCAR 40-year reanalysis project. B Am Meteorol Soc 77, 437-471.

Klein, P., Lapeyre, G., Large, W.G., 2004. Wind ringing of the ocean in presence of mesoscale eddies. Geophys Res Lett 31, doi:10.1029/2004GL020274.

Kunze, E., 1985. Near-Inertial Wave-Propagation in Geostrophic Shear. J Phys Oceanogr 15, 544-565.

Large, W.G., Crawford, G.B., 1995. Observations and simulations of upper-ocean response to wind events during the ocean storms experiment. J Phys Oceanogr 25, 2831-2852.

Lermusiaux, P.F.J., 1999. Estimation and study of mesoscale variability in the Strait of Sicily. Dynam Atmos Oceans 29, 255-303.

Lermusiaux, P.F.J., Robinson, A.R., 1999. Data assimilation via error subspace statistical estimation. Part I: Theory and schemes. Mon Weather Rev 127, 1385-1407.

Mahadevan, A., Tandon, A., 2006. An analysis of mechanisms for submesoscale vertical motion at ocean fronts. Ocean Model 14, 241-256.

Mahadevan, A., Tandon, A., Ferrari, R., 2010. Rapid changes in mixed layer stratification driven by submesoscale instabilities and winds. J Geophys Res-Oceans 115.

Mooers, C.N.K., 1975. Several effects of a baroclinic current on the cross-stream propagation of inertial-internal waves. Geophys. Fluid Dyn. 6, 245-275.

Munk, W., Wunsch, C., 1998. Abyssal recipes II: energetics of tidal and wind mixing. Deep-Sea Res Pt I 45, 1977-2010.

Palanques, A., Garcia-Ladona, E., Gomis, D., Martín, J., Marcos, M., Pascual, A., Puig, P., Gili, J.M., Emelianov, M., Monserrat, S., Guillén, J., Tintoré, J., Segura, M., Jordi, A., Ruiz, S., Basterretxea, G., Font, J., Blasco, D., Pagès, F., 2005. General patterns of circulation, sediment fluxes and ecology of the Palamo's (La Fonera) submarine canyon, northwestern Mediterranean. Prog Oceanogr 66, 89-119.

Qi, H.B., Deszoeke, R.A., Paulson, C.A., Eriksen, C.C., 1995. The Structure of near-Inertial Waves during Ocean Storms. J Phys Oceanogr 25, 2853-2871.

Salat, J., Tintore, J., Font, J., Wang, D.P., Vieira, M., 1992. Near-Inertial Motion on the Shelf-Slope Front Off Northeast Spain. J Geophys Res-Oceans 97, 7277-7281.

Santos-Muñoz, D., Martín, M.L., Luna, M.Y., Morata, A., 2006. Diagnosis and numerical simulations of a heavy rain event in the Western Mediterranean Basin. Advances in Geosciences 7, 105-108.

Skyllingstad, E.D., Smyth, W.D., Crawford, G.B., 2000. Resonant wind-driven mixing in the ocean boundary layer. J Phys Oceanogr 30, 1866-1890.

Sotillo, M.G., Ratsimandresy, A.W., Carretero, J.C., Bentamy, A., Valero, F., Gonzalez-Rouco, F., 2005. A high-resolution 44-year atmospheric hindcast for the Mediterranean Basin: contribution to the regional improvement of global reanalysis. Clim Dynam 25, 219-236.

Teague, W.J., Jarosz, E., Wang, D.W., Mitchell, D.A., 2007. Observed Oceanic Response over the Upper Continental Slope and Outer Shelf during Hurricane Ivan. J Phys Oceanogr 37, 2181-2206.

Thomas, W., Baier, F., Erbertseder, T., Kastner, M., 2003. Analysis of the Algerian severe weather event in November 2001 and its impact on ozone and nitrogen dioxide distributions. Tellus B 55, 993-1006.

Vandenbulcke, L., Rixen, M., Beckers, J.M., Alvera-Azcarate, A., Barth, A., 2008. An analysis of the error space of a high-resolution implementation of the GHER hydrodynamic model in the Mediterranean Sea. Ocean Model 24, 46-64.

Wang, D.-P., 1991. Generation and propagation of inertial waves in the subtropical front. J Mar Res 49, 619-633.

Wang, D.-P., Jordi, A., 2011. Surface frontogenesis and thermohaline intrusion in a shelfbreak front. Ocean Model 38, 161-170.

Wang, D.P., Vieira, M.E.C., Salat, J., Tintore, J., Laviolette, P.E., 1988. A Shelf Slope Frontal Filament Off the Northeast Spanish Coast. J Mar Res 46, 321-332.

Tables

Table 1. Current meter locations and depths.

Mooring	Longitude (ºE)	Latitude (ºN)	Upper level (m)	Intermediate level (m)
M2	3.2685	41.9247	-	470
M3	3.3462	41.8673	150	401
M4	3.5202	41.8455	204	495
M5	3.4646	41.8277	164	-
M6	3.4778	41.7733	ADCP (256-488 m)	
M7	3.6827	41.8897	255	478
M8	3.6778	41.6218	279	506

Table 2. Sub-inertial and near-inertial RMS error (m s^{-1}) and complex correlation coefficient (C) between observed and simulated currents averaged for each level.

Motion	Level	BASE		ASES		ESTIM	
		RMS	C	RMS	C	RMS	C
Sub-inertial	Upper	0.16	0.52	0.01	0.97	0.07	0.56
	Intermediate	0.13	0.38	0.01	0.95	0.04	0.51
	ADCP	0.21	0.58	0.01	0.98	0.07	0.75
Near-inertial	Upper	0.11	0.26	0.02	0.96	0.07	0.53
	Intermediate	0.05	0.31	0.02	0.89	0.05	0.47
	ADCP	0.05	0.34	0.02	0.90	0.04	0.52

Figure captions

Figure 1. (a) Study area within the Mediterranean Sea. (b) Bathymetry of the northwestern Mediterranean showing the real topography (gray lines), the model axes (thick black lines), and the topography used in the model (thin black lines). (c) Magnified view in the area of Palamós canyon showing the location of the current meter moorings (circles) and the topography used in the model (gray lines).

Figure 2. Comparison between time-averaged sub-inertial currents for observations (black vectors) with BASE, ESTIM and ASES runs (red vectors) at upper (left panels) and intermediate level (right panels). Scales for vectors are indicated in the first panel. The 200, 1000 and 2000 m isobaths are plotted with gray lines.

Figure 3. Comparison between near-inertial currents for observations (black vectors) with BASE, ESTIM and ASES runs (red vectors) at upper level from 10 to 21 November 2001. Vector length indicates the amplitude, vector direction shows the relative phase and the dot represents the origin. Scales for vectors are indicated in the first panel.

Figure 4. Comparison between near-inertial currents for observations (black vectors) with BASE, ESTIM and ASES runs (red vectors) at intermediate level from 10 to 21 November 2001. Vector length indicates the amplitude, vector direction shows the relative phase and the dot represents the origin. Scales for vectors are indicated in the first panel.

Figure 5. Comparison between near-inertial currents for observations (black vectors) with BASE, ESTIM and ASES runs (red vectors) at M6 measured by the ADCP from 10 to 21 November 2001. Vector length indicates the amplitude and vector direction shows the relative phase. Scales for vectors are indicated in the first panel.

Figure 6. Vertical profiles of (a) RMS error (m s^{-1}) and (b) complex correlation coefficient between observed near-inertial currents and simulated for BASE (red), ESTIM (green), and ASES (blue) runs at M6 measured by the ADCP from 10 to 21 November 2001.

Figure 7. Near-inertial vertical wavenumber spectra for the observations (black), and BASE (red), ESTIM (green), and ASES (blue) runs at M6 measured by the ADCP from 10 to 21 November 2001.

Figure 8. Time evolution of wind stress vectors for (a) BASE and (b) ESTIM runs, and (c) wind stress curl (normalized by f) at the canyon mouth (x = 60 km, y = 0 km); vectors (in oceanographic convention) are plotted every 3 h. Wind stress curl (normalized by $10^2 f$) averaged over the study period for (d) BASE and (e) ESTIM runs; the 200, 1000 and 2000 m isobaths are plotted with gray lines.

Figure 9. Clockwise spectral density (10^3 kg^2 m^{-2} s^{-3}) for the wind stress at the canyon mouth (x = 60 km, y = 0 km) used in BASE (black line) and ESTIM (red line). Vertical gray lines are inertial (18 h) and semidiurnal (12 h) periods.

Figure 10. Time evolution of ESTIM near-inertial currents and sub-inertial relative vorticity (normalized by f) at a cross-shore section located at y = 0 km. Vector length indicates the amplitude, vector direction shows the relative phase and the dot represents the origin. Vectors are resampled onto a grid with a spacing of 8 km in the horizontal and 40 m in the vertical, and amplitudes below 3 cm/s are not represented. Scales for vectors and vorticity are indicated in the first panel. The 28.2, 28.4, 28.6, and 28.8 isopycnals (from top to bottom, in σ_θ units) are represented with gray lines.

Figure 11. Time evolution of ASES near-inertial currents and sub-inertial relative vorticity (normalized by f) at a cross-shore section located at y = 0 km. Vector length

indicates the amplitude, vector direction shows the relative phase and the dot represents the origin. Vectors are resampled onto a grid with a spacing of 8 km in the horizontal and 40 m in the vertical, and amplitudes below 3 cm/s are not represented. Scales for vectors and vorticity are indicated in the first panel. The 28.2, 28.4, 28.6, and 28.8 isopycnals (from top to bottom, in σ_θ units) are represented with gray lines.

Figure 12. Time evolution of SUBMS near-inertial currents and sub-inertial relative vorticity (normalized by *f*) at a cross-shore section located at y = 0 km. Vector length indicates the amplitude, vector direction shows the relative phase and the dot represents the origin. Vectors are resampled onto a grid with a spacing of 8 km in the horizontal and 40 m in the vertical, and amplitudes below 3 cm/s are not represented. Scales for vectors and vorticity are indicated in the first panel. The 28.2, 28.4, 28.6, and 28.8 isopycnals (from top to bottom, in σ_θ units) are represented with gray lines.

Figure 1

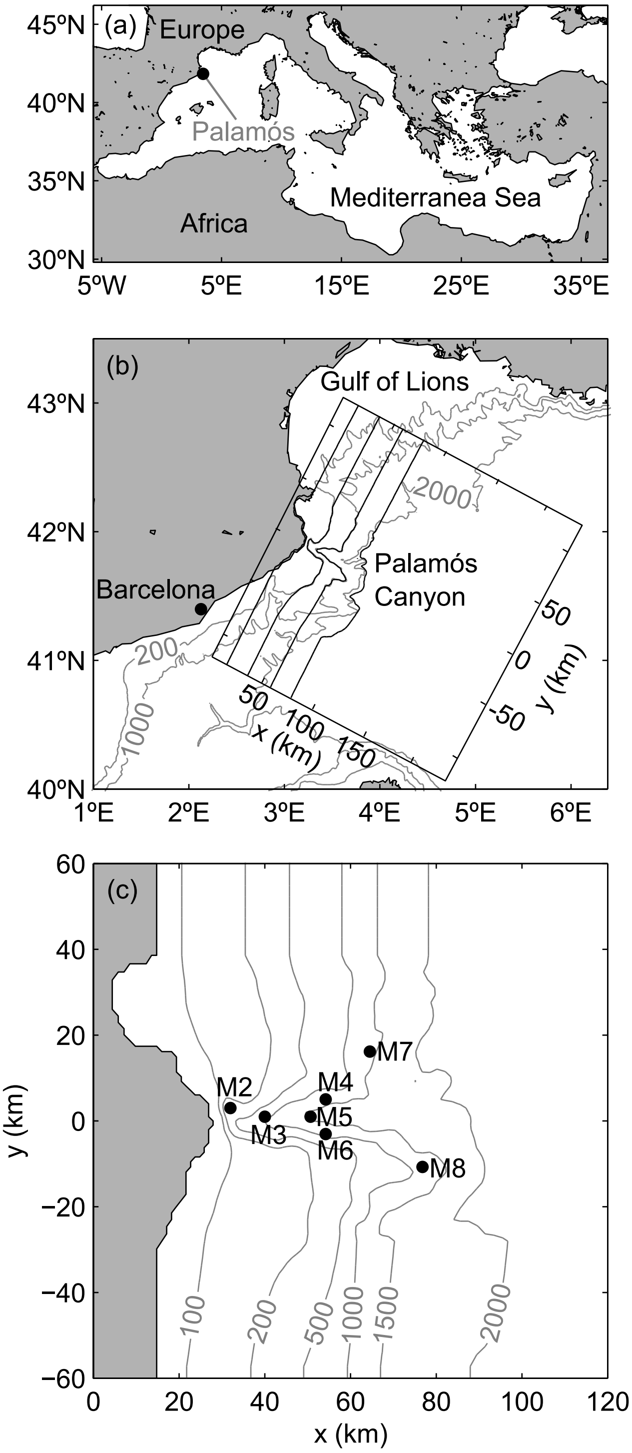
(a)
Europe
Palamós
Mediterranea Sea
Africa
45ºN
40ºN
35ºN
30ºN
5ºW
5ºE
15ºE
25ºE
35ºE
(b)
Gulf of Lions
2000
Palamós
Canyon
Barcelona
200
1000
50
100
150
x (km)
50
0
-50
y (km)
43ºN
42ºN
41ºN
40ºN
1ºE
2ºE
3ºE
4ºE
5ºE
6ºE
(c)
M2
M3
M4
M5
M6
M7
M8
100
200
500
1000
1500
2000
60
40
20
0
−20
−40
−60
y (km)
0
20
40
60
80
100
120
x (km)

Figure 2

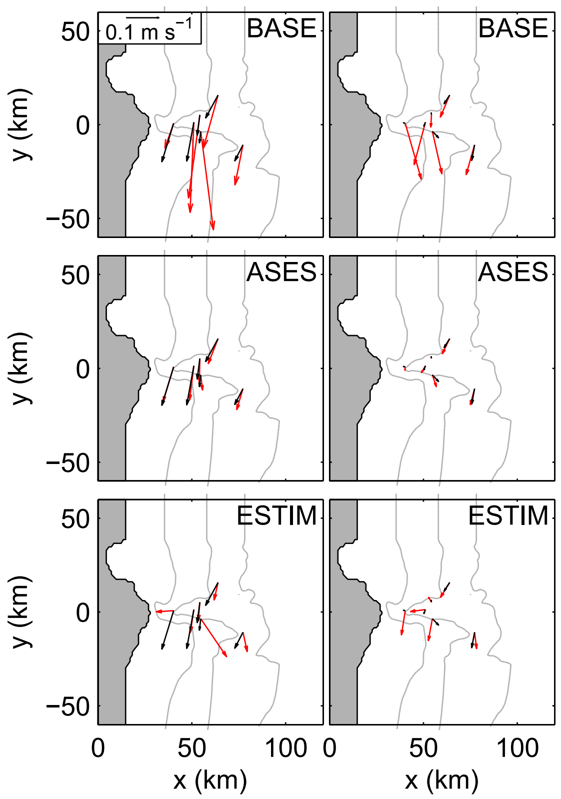

0.1 m s^{-1}
BASE
BASE
ASES
ASES
ESTIM
ESTIM
50
0
−50
y (km)
y (km)
y (km)
0
50
100
x (km)
x (km)

Figure 3

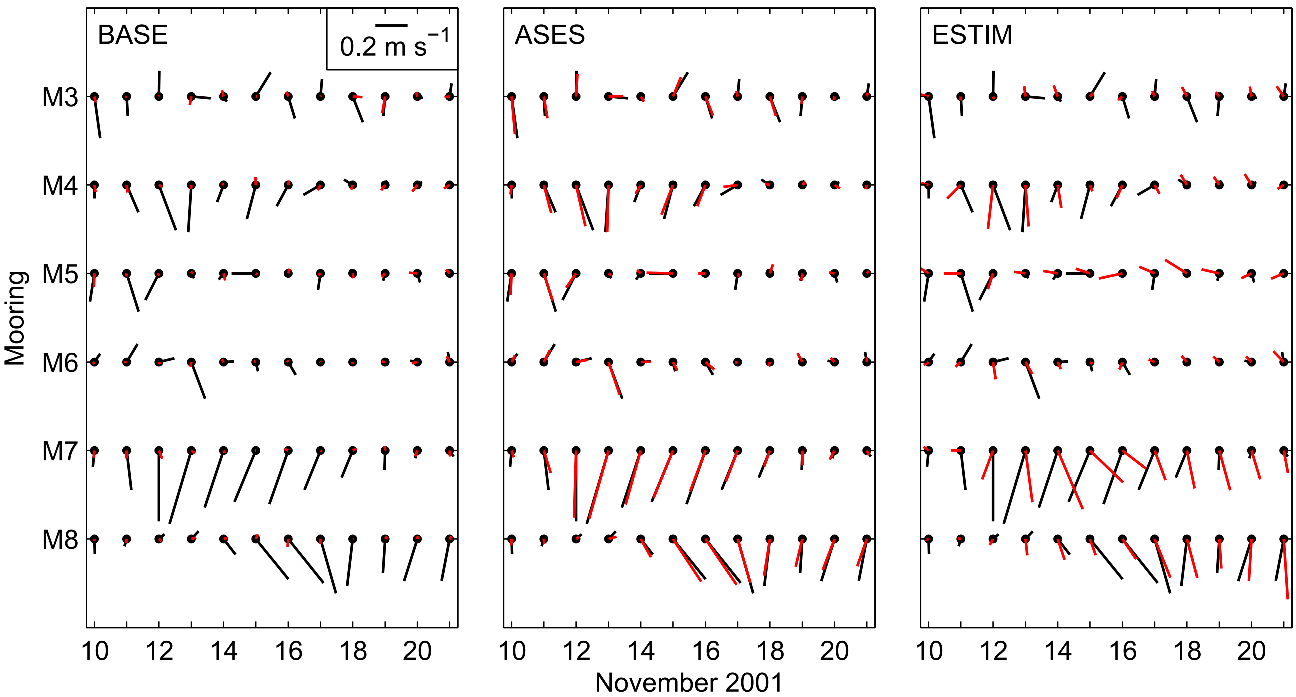
BASE
0.2 m s^{-1}
ASES
ESTIM
M3
M4
M5
M6
M7
M8
Mooring
10
12
14
16
18
20
November 2001

Figure 4

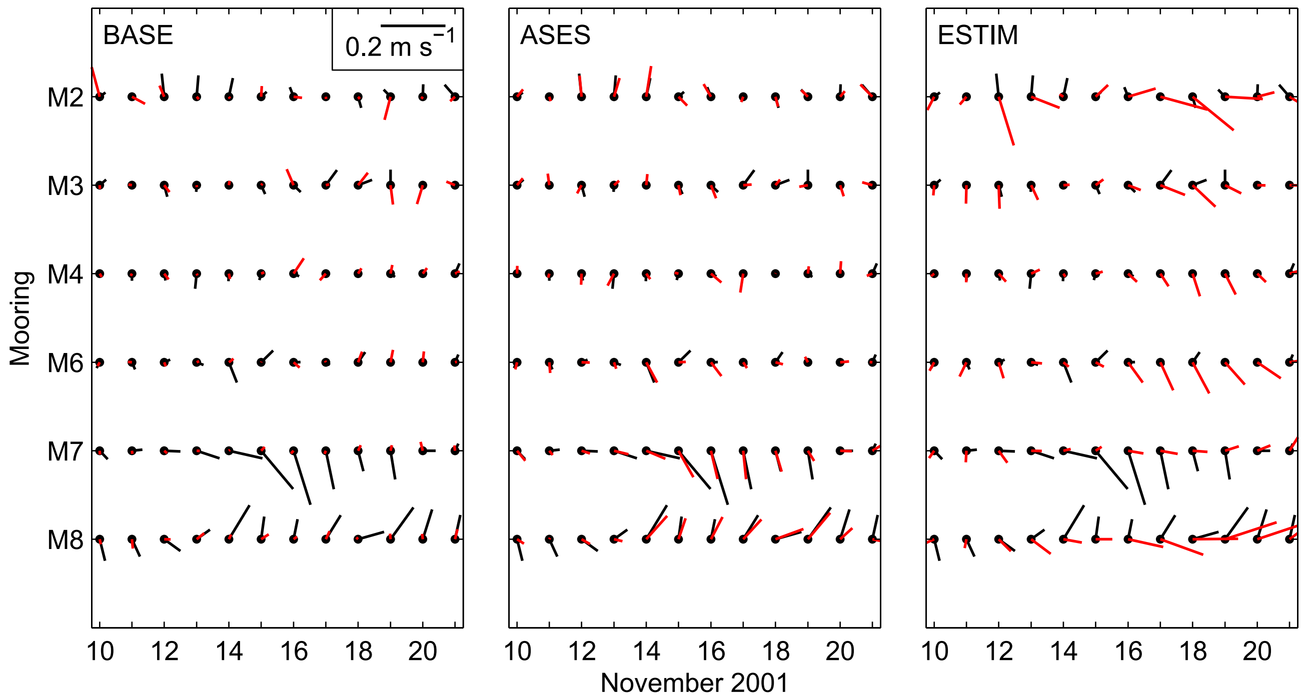
BASE
0.2 m s^{-1}
ASES
ESTIM
M2
M3
M4
M6
M7
M8
Mooring
10
12
14
16
18
20
November 2001

Figure 5

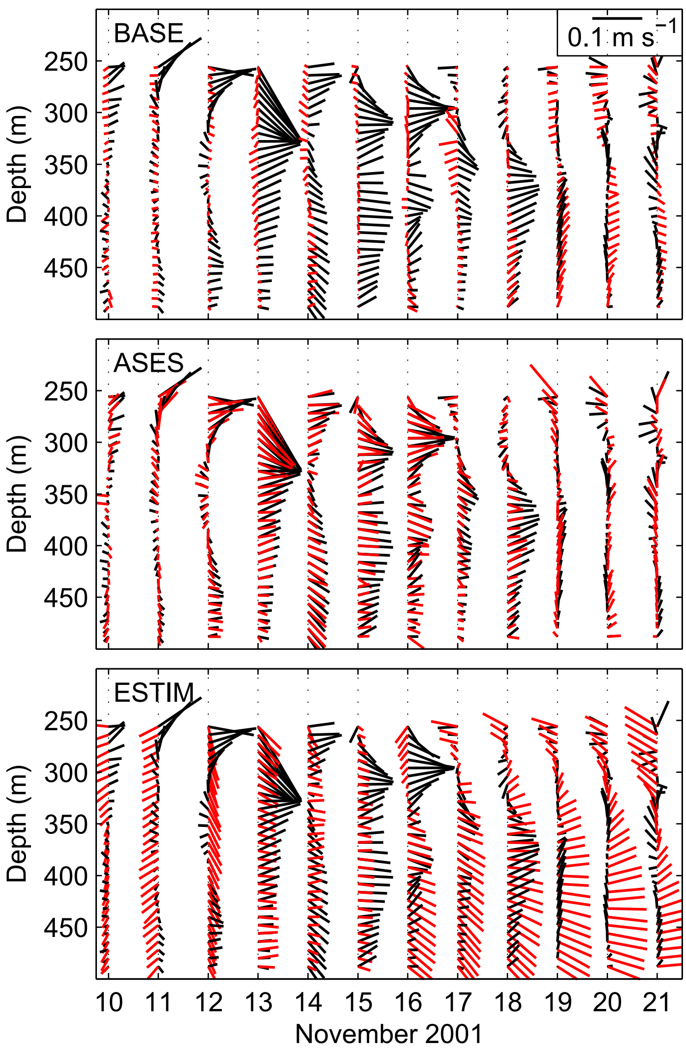
BASE
0.1 m s^{-1}
ASES
ESTIM
Depth (m)
250
300
350
400
450
10 11 12 13 14 15 16 17 18 19 20 21
November 2001

Figure 6

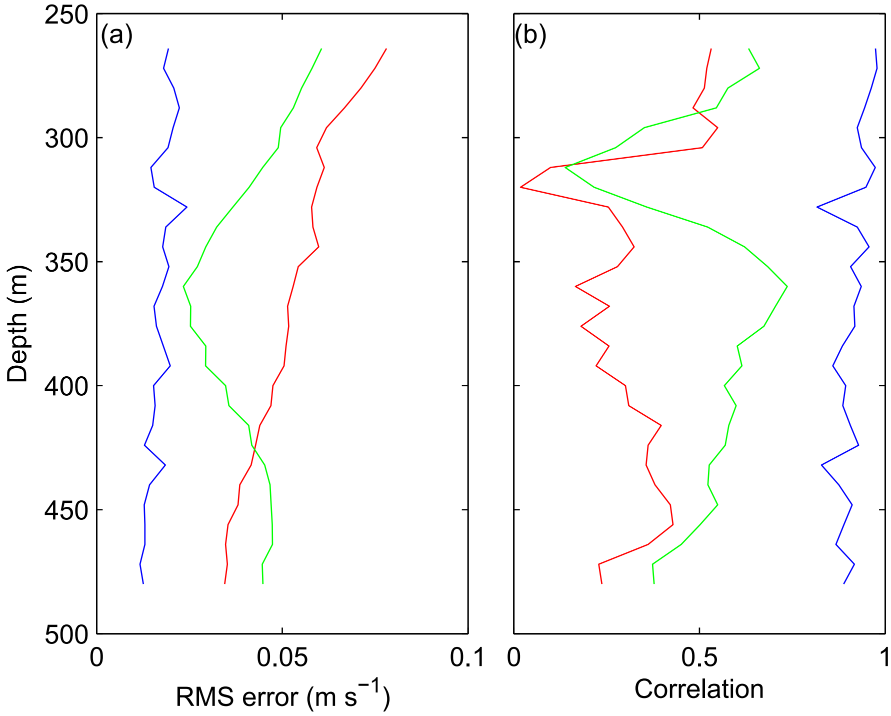

(a)
(b)
Depth (m)
250
300
350
400
450
500
0
0.05
0.1
RMS error (m s^{-1})
0
0.5
1
Correlation

Figure 7

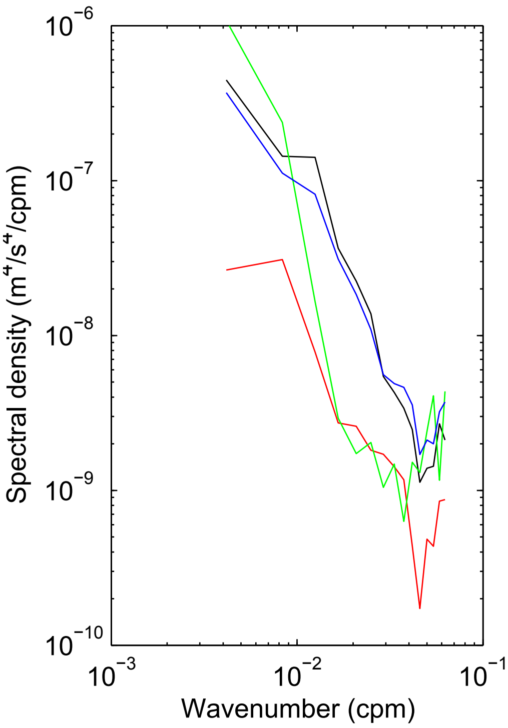
10^{-6}
10^{-7}
10^{-8}
10^{-9}
10^{-10}
Spectral density (m^4/s^4/cpm)
10^{-3}
10^{-2}
10^{-1}
Wavenumber (cpm)

Figure 8

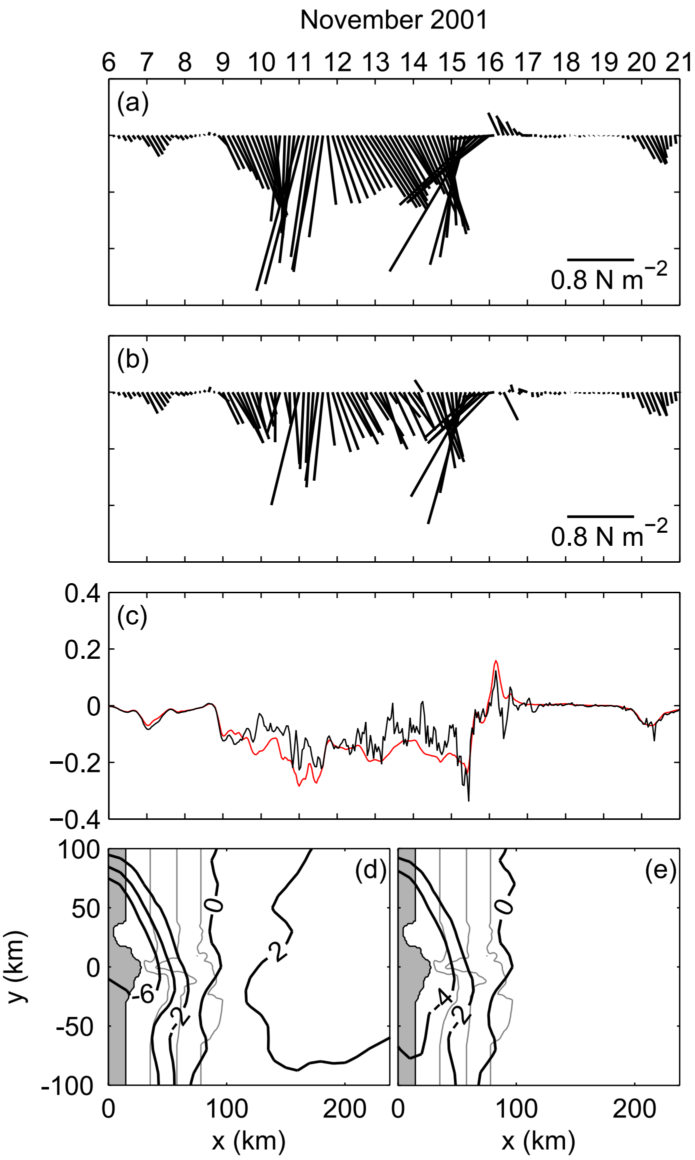

November 2001
6 7 8 9 10 11 12 13 14 15 16 17 18 19 20 21
(a)
0.8 N m^{-2}
(b)
0.8 N m^{-2}
0.4
0.2
0
−0.2
−0.4
(c)
100
50
0
-50
-100
y (km)
(d)
-6
-2
0
2
(e)
-4
-2
0
0 100 200
x (km)
0 100 200
x (km)

Figure 9

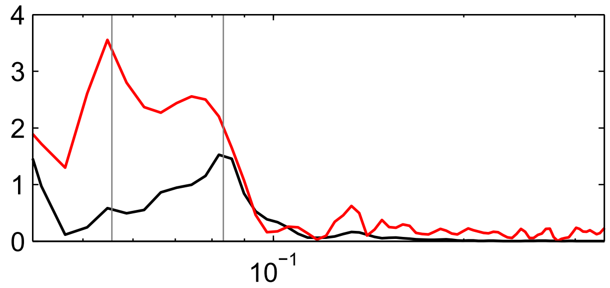

Figure 10

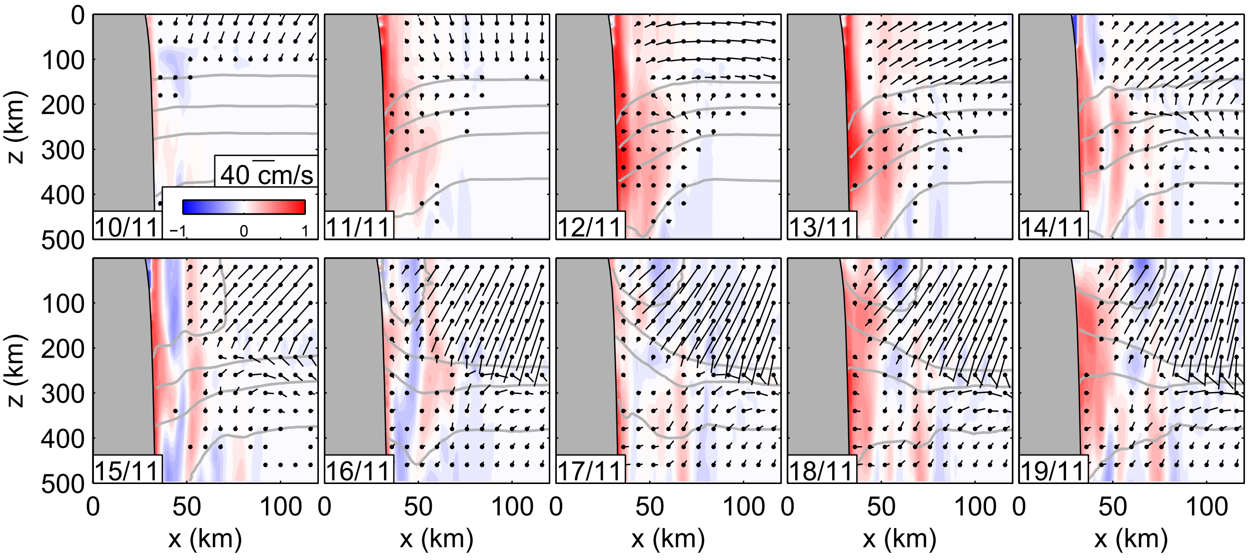

10/11
11/11
12/11
13/11
14/11
15/11
16/11
17/11
18/11
19/11
40 cm/s
−1
0
1
z (km)
x (km)
0
100
200
300
400
500
0
50
100

Figure 11

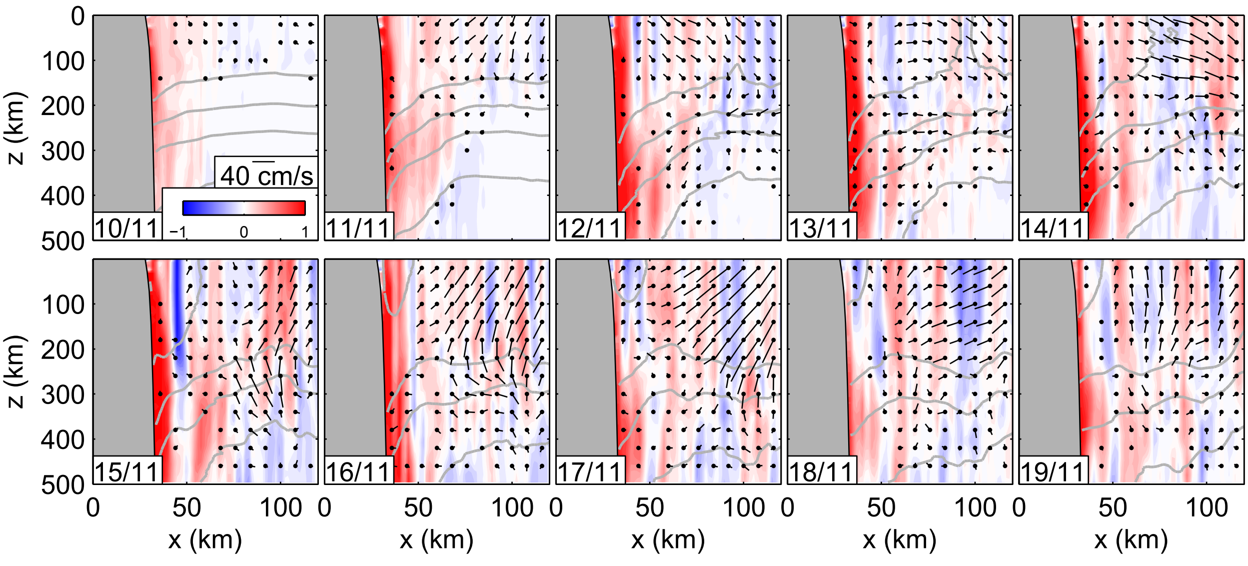

z (km)
x (km)
40 cm/s
10/11
11/11
12/11
13/11
14/11
15/11
16/11
17/11
18/11
19/11

Figure 12

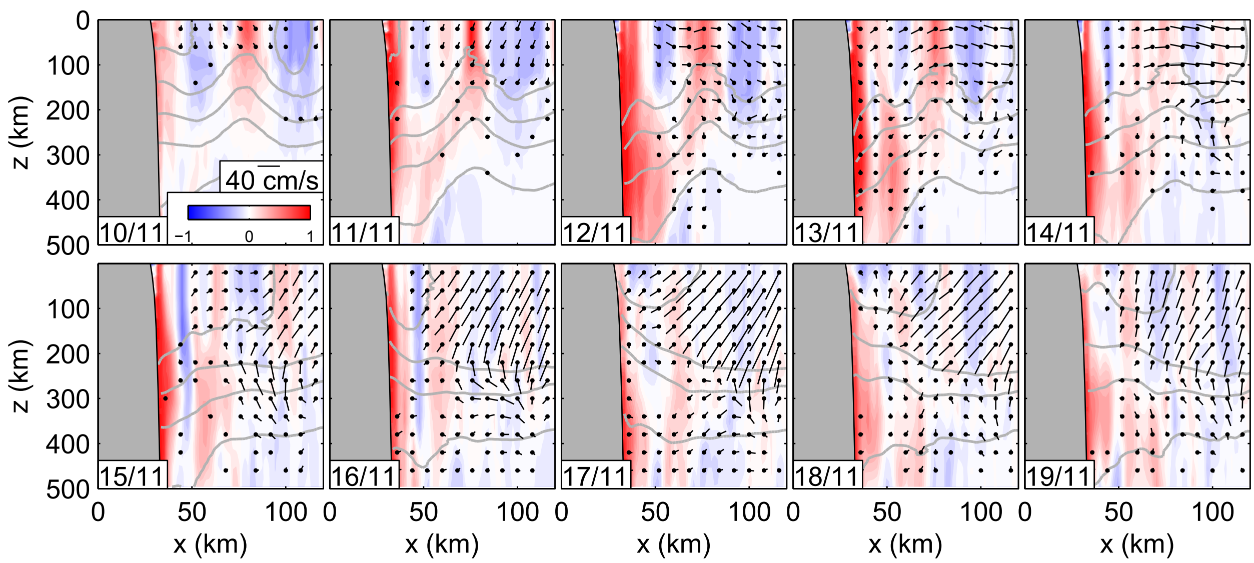

z (km)
0
100
200
300
400
500
40 cm/s
−1
0
1
10/11
11/11
12/11
13/11
14/11
15/11
16/11
17/11
18/11
19/11
0
50
100
x (km)